Cracking during thermal post-processing of laser powder bed fabricated CM247LC Ni-superalloy

Boswell, John H.; Clark, Daniel; Li, Wei; Attallah, Moataz M.

DOI:
10.1016/j.matdes.2019.107793

Document Version
Publisher's PDF, also known as Version of record

Citation for published version (Harvard):
Boswell, JH, Clark, D, Li, W & Attallah, MM 2019, 'Cracking during thermal post-processing of laser powder bed fabricated CM247LC Ni-superalloy', *Materials and Design*, vol. 174, 107793.
https://doi.org/10.1016/j.matdes.2019.107793

Materials and Design 174 (2019) 107793

Contents lists available at ScienceDirect

Materials and Design

journal homepage: www.elsevier.com/locate/matdes

Cracking during thermal post-processing of laser powder bed fabricated CM247LC Ni-superalloy

John H. Boswell [a], Daniel Clark [a], Wei Li [a], Moataz M. Attallah [b,*]

[a] Rolls-Royce, PO Box 31, Derby DE24 8BJ, United Kingdom

[b] University of Birmingham, School of Metallurgy and Materials, Edgbaston, Birmingham B15 2TT, United Kingdom

HIGHLIGHTS

- Cracking due to post-processing of laser fabricated Ni-superalloys was studied.
- Mechanisms were associated with different heat treatment temperatures.
- The mechanisms are ductility dip cracking and strain age cracking.
- Microstructural evidence was obtained to elucidate the cracking mechanisms.

GRAPHICAL ABSTRACT

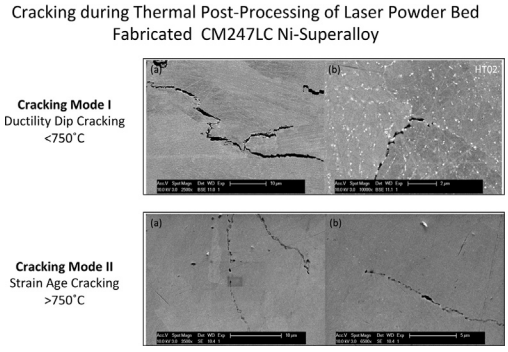

ARTICLE INFO

Article history:
Received 4 November 2018
Received in revised form 31 March 2019
Accepted 9 April 2019
Available online xxxx

Keywords:
Nickel superalloys
Laser powder bed fusion
Microstructure
Mechanical properties

ABSTRACT

The causes of cracking during thermal post-processing of laser powder bed fabricated (LPBF) CM247LC Ni-superalloy have been examined. Micro-hardness measurements and microstructural analyses were undertaken following short aging heat treatments around the phase transformation temperatures identified by Differential Scanning Calorimetry (DSC) analysis of the as-built condition. Results showed a steep increase in cracking density in the samples between 450 °C and 600 °C, which corresponded to changes in the microstructure, hardness, and elastic modulus. A combination of ductility dip cracking and strain age cracking mechanisms were identified as the primary causes of cracking in LPBF CM247LC following post-build thermal treatments. The results of this work shed light on the relationship between the heat treatment temperatures and the onset of post-build cracking, and could help develop post-LPBF heat treatments for high γ′ Ni-superalloys.

1. Introduction

CM247LC is a Ni-base superalloy which can be used in directionally solidified (DS) or poly-crystalline (PX) forms, The alloy has a high γ′ volume fraction in the order of 67% in the fully heat treated condition [1]. The elevated temperature mechanical properties, oxidation and corrosion resistance of this alloy represent the optimum that can be achieved with conventionally cast alloys, which makes it attractive for additive manufacture of high performance gas turbine components [2].

Manufacture of this alloy is intrinsically difficult due to its complex chemistry and high γ′-content [3], which is necessary to achieve the required elevated temperature strength and creep resistance [1,4]. CM247LC is classified as non-weldable due to the high Ti + Al content, making it susceptible to Strain-Age (reheat) Cracking (SAC). It is particularly prone to microcracking during laser powder bed fusion (LPBF)

* Corresponding author.
E-mail address: m.m.attallah@bham.ac.uk (M.M. Attallah).

https://doi.org/10.1016/j.matdes.2019.107793

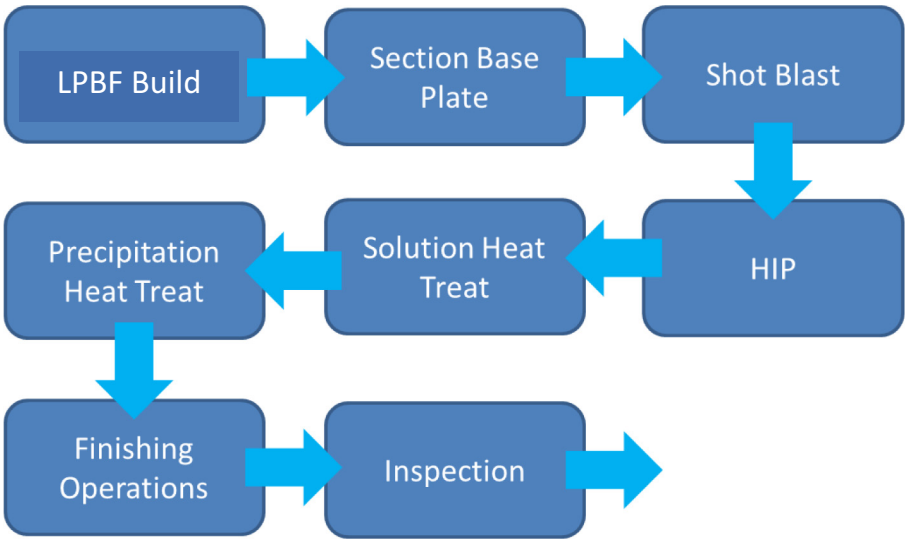

Fig. 1. Schematic diagram for the manufacturing route for high γ′ content nickel superalloys [13,14].

process (also known as Selective Laser Melting, SLM) [5–7]. Several studies have investigated the effects of LPBF parameters on micro-cracking during LPBF build, which have identified process windows where acceptable levels of micro-cracking can be achieved [8–10]. Subsequent hot isostatic pressing (HIP) can close internal micro-cracks [11], however; large residual stresses induced during building often lead to macro-cracking during the HIP process [12].

The current manufacturing route for Ni-superalloys LPBF is illustrated schematically in Fig. 1, typically HIP cycle durations up to 4 h are used followed by a solution heat treatment above the γ′ solvus temperature for 2 h and a single stage age at 870 °C for 16 h [9,13,14].

LPBF built high γ′ nickel-base superalloys are susceptible to SAC during post build heat treatment, as proposed by Etter & Kuenzler. [15] who investigated LPBF of IN738. Furthermore, materials such as IN738 and CM247LC have extremely low ductility at temperatures above between $0.4T_m$ and $0.7\ T_m$, which can lead to inter-granular cracking within this temperature range, which is referred to as Ductility Dip Cracking (DDC) [16]. The factors that affect DDC susceptibility as described by Collins and Lippold include: grain size, alloy composition, impurities, grain boundary segregation, precipitation, grain boundary pinning by carbides and borides, crystallographic orientation, relative to the applied stress, grain tortuosity and dynamic recrystallisation [16]. Comparatively, DDC and SAC differ in that SAC is mainly associated with weld reheat, which could happen for a material with a low precipitates content either during post-LPBF heat treatments that initiate γ′ precipitation, leading to cracking through the reduction in ductility combined with the pre-existing residual stresses, or due to the in-process reheating and repeated thermal cycling during LPBF that leads to cracking through the same (strain-age) mechanism. Conversely, DDC is caused by the aforementioned microstructural factors that result in a reduced ductility when loaded in a specific temperature range ($0.4–0.7\ T_m$), leading to crack initiation. Thus, the main difference is the association of SAC with both precipitation and residual stresses.

This paper investigates the phase transformations that occur during the heat-up portion of the post-LPBF HIP or stress relief cycles and identifies the microstructural changes that coincide with a step change in the crack density of the alloy samples in order to elucidate the microstructural causes for cracking during post-processing.

Table 1
Range of parameters used in design of experiments optimisation.

Material	Laser power range/W	Scan speed range/mms^{-1}	Layer thickness/μm	Hatch spacing range/mm
CM247LC	100–200	400–2000	20	0.03–0.08

2. Experimental

A single 15 mm diameter rod sample was built in an argon atmosphere with O_2 levels below 300 ppm on EOS M280 LPBF machine using optimised melting parameters designed to minimise levels of micro-cracking, which are based on the work of Carter et al. [17]. The parameter limits used in the experiments are listed in Table 1. The rod was then cut into 10 mm long sections, Fig. 2.

Differential scanning calorimetry (DSC) was carried out on an as built CM247LC sample to identify the phase transformations within the temperature range of a typical HIP cycle. Analysis was carried out using the Netzsch DSC404C equipment and analysed using the Netzsch STA 449C software. Heat up rate for DSC analysis was 10 °C/min under an argon atmosphere at atmospheric pressure, with a constant flow rate of 100 cc/min and charge weight is between 32 and 93 mg. The heat up rate during HIP of conventional heat treatment furnaces is typically 5–10 °C/min, which is representative to the sample heating up rate used in DSC analysis.

Following DSC analysis, a series of short aging experiments were carried out at temperatures that were chosen based on the results of the DSC analysis. All heat treatments were carried out in air in a box furnace

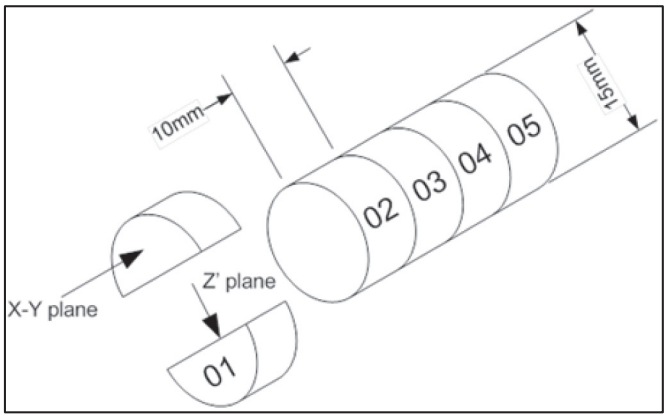

Fig. 2. Sectioning of heat treatment specimens; both the X-Y plane, perpendicular to build, and Z-plane, parallel to build, were examined using post-process thermal treatment.

Table 2
Post build heat treatment experiments LPBF CM247LC.

Sample	Hold temperature (°C)
HT01	450
HT02	600
HT03	700
HT04	750
HT05	850
HT06	975

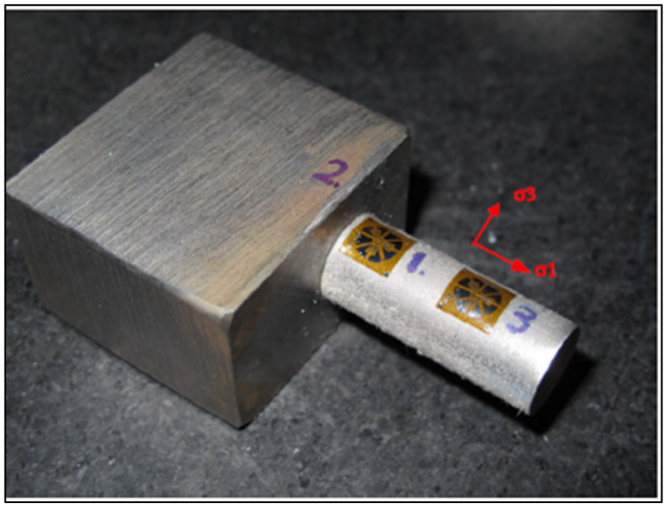

Fig. 3. Strain gauge positions on the as-built CM247LC samples.

Table 3
Elastic modulus values used in residual stress calculations [20].

Modulus	Measured values (GPa)
$E_{vertical}$	159.2
$E_{horizontal}$	157.7
$E_{45\ Deg}$	195
G	90

using a set heat up rate of 9 °C/min, followed by a 2 h soak at the hold temperatures shown in Table 2.

Samples were mounted in conductive Bakelite and ground using silicon carbide papers from 250 to 4000 mesh, diamond polished from 9 μm to a 1 μm and then final polished using 0.25 μm colloidal silica (OPS).

Residual stress measurements were carried out by Stresscraft Ltd. using target strain gauge measurement, ASTM E837 [18]. Strain gauges were placed at equally spaced locations along the length of 15 mm dia. x 30 mm long test bars and samples were measured attached to a section of the baseplate, Fig. 3. Gauges were aligned parallel (0°), perpendicular (90°) and 225° from the build direction (Z-plane), all 3 strain components were measured to determine the residual stress. Orbital drilling was carried out at the centre of each strain gauge at increments of 4 × 16 μm, 4 × 32 μm and 8 × 64 μm to a depth of 0.7 mm. Stress data was generated to a depth of 512 μm [19].

Anisotropic elastic modulus values were used to calculate the residual stresses as per ASTM E837 in the hoop, σ3, and build direction, σ1, as listed in Table 3. The elastic modulus measurements were measured using the impact excitation method (ASTM E1876) for temperatures between 20 °C and 1000 °C at 50 °C increments. A Poisson's ratio of 0.3 was used. The elastic modulus values were taken from measurements from as-built LPBF samples and were provided by the National Physical Laboratory (NPL), UK [20].

Micro-hardness testing using the Vickers hardness indenter and a 1 kg load, HV(1), was carried out on each sample using the Struers automatic hardness tester. 25 measurements were taken from each sample to obtain a statistical spread of data. Measurements were carried out across the full width of the sample on the cross section parallel to the build direction and perpendicular to the build direction.

Optical microscopy was carried out using a Zeiss optical microscope fitted with a camera and automated stage. Mosaic images of the as polished samples 1 to 6 were produced at an appropriate magnification to quantify the crack density (expressed in μm/mm^2) using ImageJ© software. Samples were imaged in both parallel and perpendicular to the build plane, collecting an average of 40 measurements, 20 in the Z-plane and 20 in the X-Y plane.

SEM analysis was performed using a Philips XL-30 field emission gun (FEG) electron microscope, equipped with energy dispersive spectroscopy (EDS).

Thermo-Calc® (phase diagram thermodynamic simulation software) was used to define the equilibrium phase content for a nominal composition CM247LC powder, see Table 4, using a maximum oxygen content of 200 ppm. The TCNI8 database was used in the simulation.

Scheil analysis was used to determine the sequence of the phase formation, phases formed and their mole fraction during solidification. The Scheil analysis assumes no diffusion in solid phase during solidification and infinite diffusion in the liquid phase [21].

3. Results and discussions

3.1. DSC analysis

DSC analysis was used to identify the phase transformations associated with the ductility drop temperature range, which occurs typically between 500 °C and 1000 °C. The DSC trace showed 2 distinct exothermic reactions; the first reaction is in the temperature range 450 °C to 700 °C and the second reaction starts at 740 °C and continues to 975 °C, Fig. 4.

The reactions have been associated with γ′ precipitation (either at grain boundaries or growth of intergranular γ′) and diffusion of Cr to grain and cell boundaries. Diffusion of Cr to grain and cell boundaries is likely to be due to transformation of MC carbides to M_6C and $M_{23}C_6$, which is also accompanied by growth of the γ′ phase in these regions [22].

3.2. Residual stress

A peak value of Von Mises stress of 1134 MPa at a depth of 352 μm was calculated based on the axial and hoop stress σ1 and σ3, Fig. 5. The measurements are for strain gauge position 1 (Fig. 3), close to the base of the sample. The Von Mises stress is greater than the yield stress for cast CM247LC reported by Kim et al. [23]. The strain gauge measurements are likely to be affected by plastic deformation during drilling and the material anisotropy, which are likely to affect the values obtained

Table 4
CM247LC nominal alloy composition wt% (courtesy of Cannon-Muskegon Inc.).

Elements	C	Cr	Ni	Co	Mo	W	Ta	Ti	Al	B	Zr (Max)	Hf	Si (max)
CM247LC	0.07	8	Bal	9	0.5	10	3.2	0.7	5.6	0.01	0.03	1.4	0.1

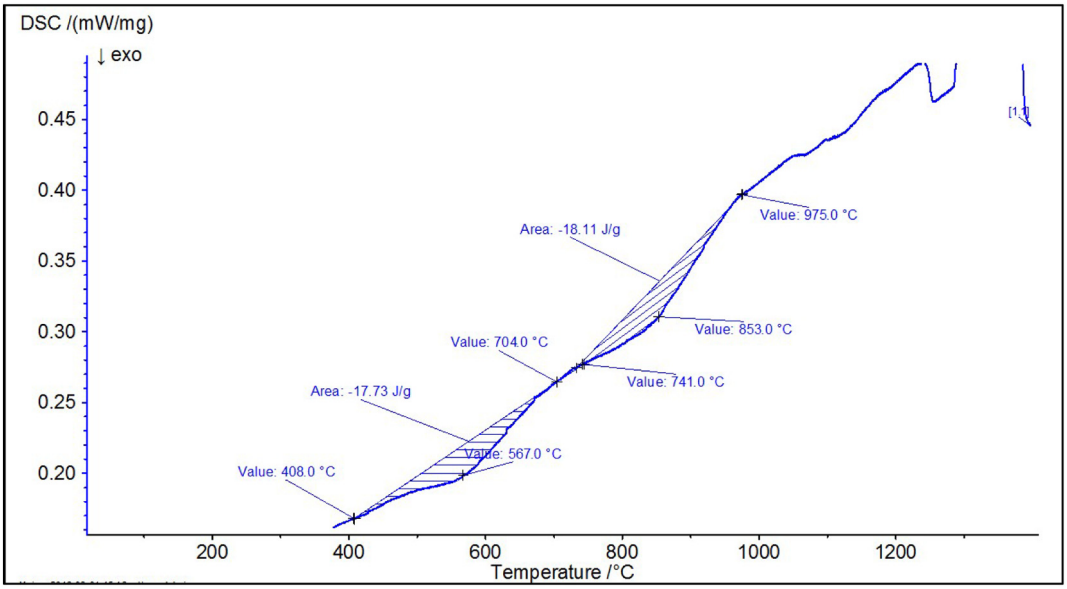

Fig. 4. DSC analysis showing DSC plot and selected heat treatment temperatures.

[19], however the results do indicate the large magnitude of the stresses resulting from the LPBF process.

A study of residual stress in LPBF by Mercelis and Kruth [24] showed that the as-built residual stresses are in the range of the material yield stress. However, the residual stresses are reduced after removal from the baseplate. Therefore, although no further measurements were made, the residual stress in the test bar used in the experiments will be lower than the values presented in Fig. 5. Furthermore at temperatures above 650 °C the strength of the tool steel base reduces significantly, compared to the build itself. Therefore, at the higher heat treatment temperatures, the baseplate would have negligible effect on residual stress [25].

3.3. Micro-hardness measurements

Micro Vickers hardness is plotted as a function of annealing temperature in Fig. 6. The error bars shown represent the 95% confidence interval for the mean hardness value and is calculated using the equation:

$$95\%\text{C.I.} = 1.96\left(\frac{\sigma}{\sqrt{N}}\right)$$

where σ is the standard deviation of the micro-hardness measurements and N is the number of measurements taken for each sample.

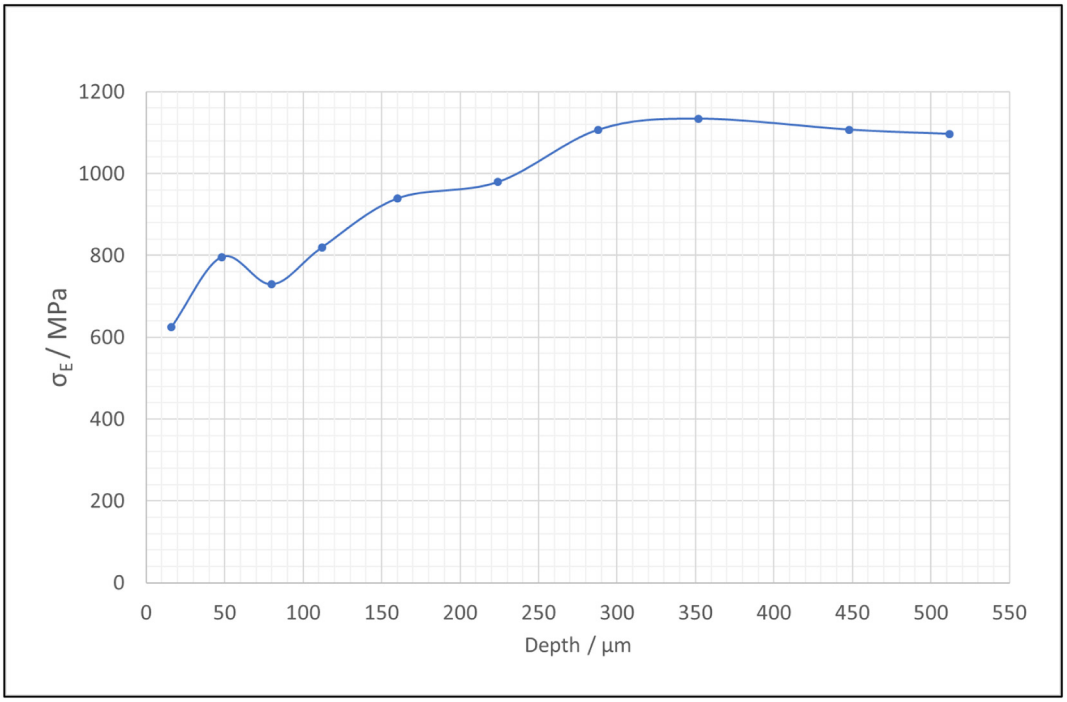

Fig. 5. Residual stress represented by Von Mises stress in LPBF CM247LC builds.

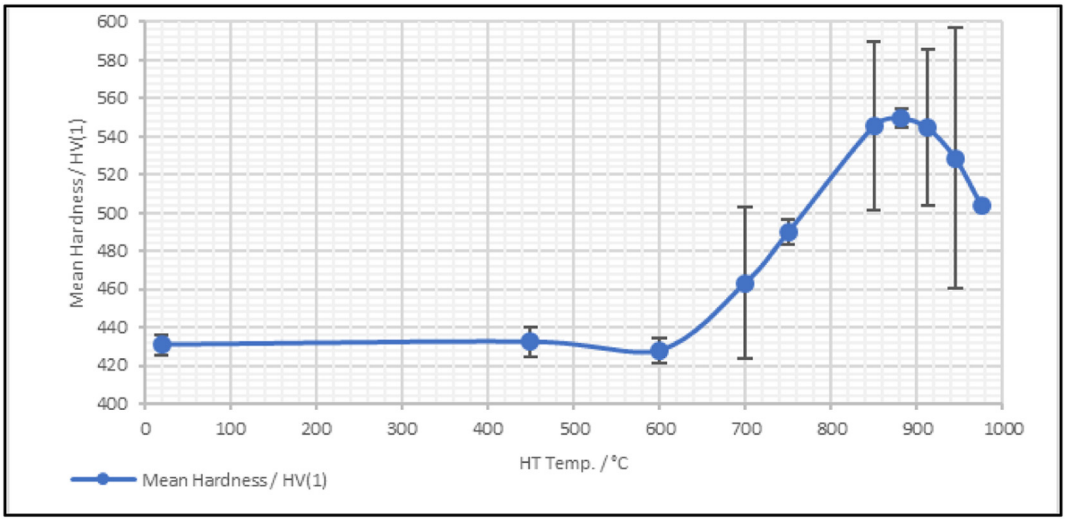

Fig. 6. Mean Vickers micro-hardness HV(1) for samples heat treated for 2 h at a range of temperatures between 450 °C and 975 °C.

There is no increase in room temperature hardness in the samples heat treated below 700 °C, with a peak hardness achieved after aging at 882 °C; above this temperature hardness begins to drop [26]. The temperature range which results in increases in the room temperature hardness is coincident with the second exothermic reaction identified in Fig. 4, no change in hardness is associated with the first exothermic reaction between 450 °C and 700 °C. The figure shows there is an increase in scatter in the hardness data above 700 °C, although scatter, represented by the confidence interval, is low for the samples heat treated at 750 °C and 880 °C. Scatter increases above 914 °C.

3.4. Crack density measurements

Crack density, shown in Fig. 7, decreases with the increase in the annealing temperature, which is opposite to the trend between the hardness and annealing temperature (Fig. 6). The minimum value for crack density was recorded in HT05, which was heat-treated for 2 h at 850 °C. By contrast the highest value for crack density was measured in sample HT02, which was heat-treated for 2 h at 600 °C. Both stress relief and γ′-precipitation occur at higher rates at temperatures >750 °C, which is likely to have resulted in a relatively lower crack density (and less scatter) and higher hardness in the samples treated at high annealing temperatures.

The variation in crack density is demonstrated by the thresholded images used in the crack density analysis, Fig. 8. The images also show lack of fusion voids, which were filtered out of the crack analysis by defining the circularity and aspect ratios so that they are no counted as cracks.

3.5. Microstructure

The microstructure for samples heat-treated below 700 °C shows a cellular dendritic morphology typical of LPBF, with fine cellular γ dendrites interspersed with carbides at cell and grain boundaries. No γ′ was visible (using the SEM resolution) in the microstructure of the samples that were heat treated within the 408 °C to 704 °C temperatures range, even at high magnification. Previous studies of LPBF CM247LC have identified very fine γ′, approximately 5 nm diameter, precipitates identified by dark field TEM imaging [4,9].

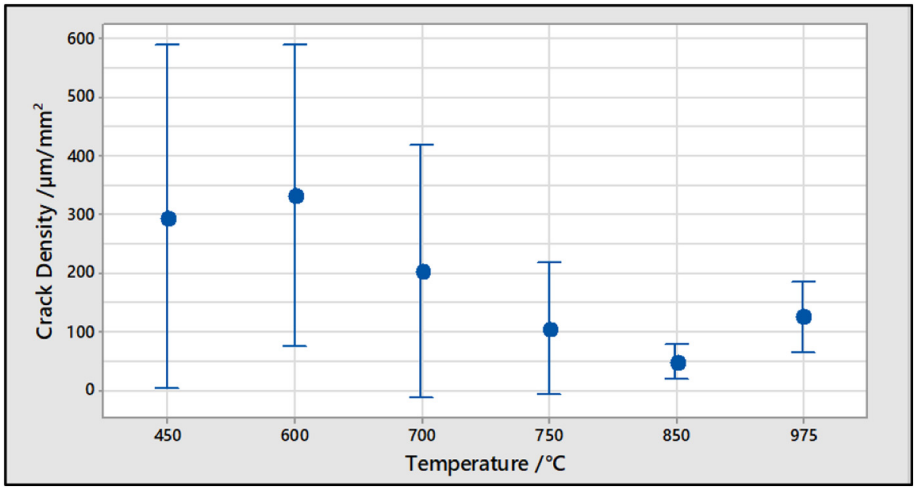

Fig. 7. Crack density (µm/mm^2) for 2 h heat treatments between 450 °C and 975 °C.

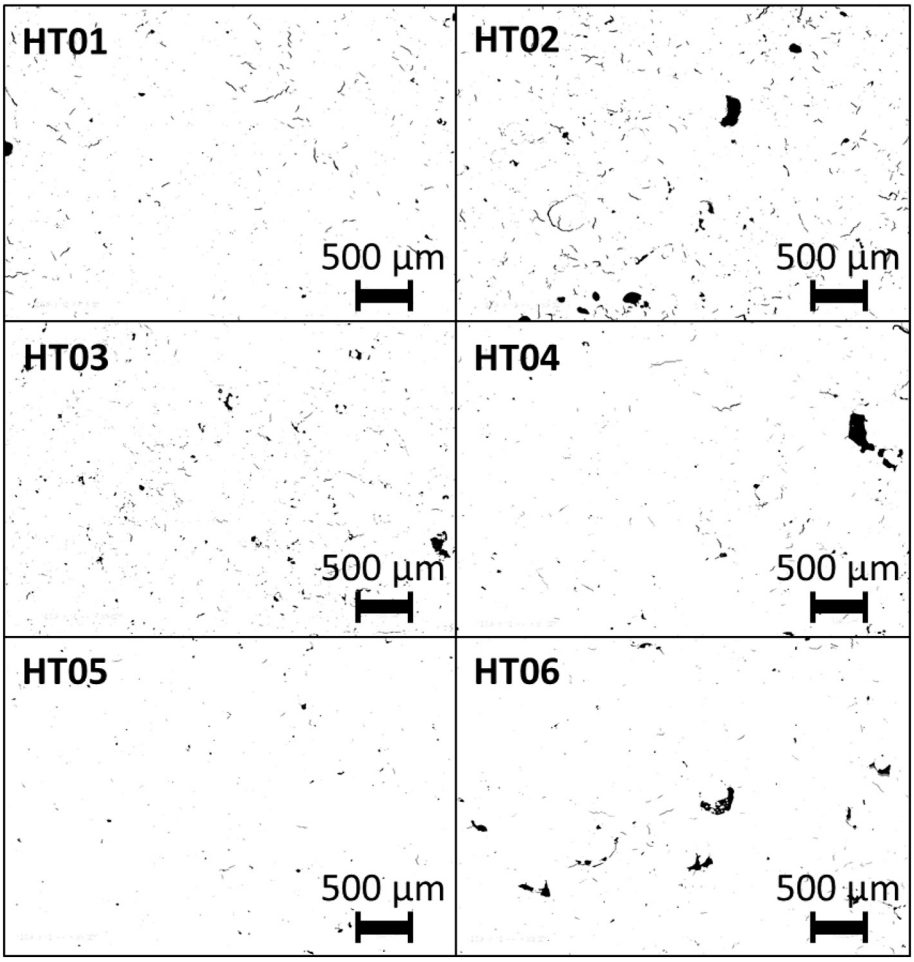

Fig. 8. Optical micrographs showing the variation in crack density for samples HT01 to HT06.

Heat treatments above 750 °C up to 975 °C are characterised by a change in the contrast of the cells when observed using backscattered electrons imaging in Fig. 8(c), combined with the precipitation of fine intra-cellular γ′, γ′ films at cell and grain boundaries and $M_{23}C_6$ carbides at grain boundaries.

The transformation of MC carbides + γ to $M_{23}C_6$ + γ′ is observed in cast CM247LC [27]. Evidence indicates that the same transformation occurs in LPBF CM247LC and is identified through the microstructural changes observed in the heat-treated samples. No obvious phase transformations are identified in the specimen's heat treated below 700 °C, Fig. 9(a) and 9(b). At 750 °C there are changes in contrast between clumps of adjacent cells and very fine precipitates are visible at cell boundaries, Fig. 9(c). The sample heat-treated at 850 °C, Fig. 9(d), exhibited a distinctive secondary phase at cell boundaries, a very fine precipitate phase, and blocky carbides at the fractured grain boundary. Due to the very high cooling rates associated with LPBF [28], the as built material has a fine cellular microstructure, Fig. 9(a) shows γ cells surrounded by MC carbides and γ/γ′ eutectic [4]. Precipitation and growth of the γ′ phase is evident at 750 °C around cell and grain boundaries, Fig. 9(c), which is the result of micro-segregation during solidification [29], typically due to low partition coefficient elements, such as Al. Studies carried out by Divya et al. [9], identified Al-concentrations at cell boundaries through TEM analysis, but did not conclude that Al was associated with the γ/γ′ eutectic phase. However, TEM diffraction studies by Wang et al. [4] identified the presence of γ/γ′ eutectic at cell boundaries, which is consistent with the solidification behaviour of cast Ni-base superalloys [30].

3.6. EDS analysis

Line scans taken across the cell boundaries shown in Fig. 10(a) show concentrations of Hf and Al at cell boundaries. The concentration of these elements is due to the presence of Hf-rich carbides and γ/γ′ eutectic in the inter-cellular and inter-granular regions of the microstructure [4,9]. No changes in the concentration of Al and Hf across the cell boundary were identified in the sample heat treated at 975 °C, however a peak in Cr was identified at the grain boundary providing evidence of the transformation of MC carbides to $M_{23}C_6$ plus γ′, Fig. 10(b). The MC carbide transformation is likely to occur during the 2 h soak above 700 °C, which overlaps with the temperature range of the γ′ transformations shown as exothermic peaks in the DSC analysis in Fig. 4. The DSC heating rate is 10 °C/min, which means the dwell time at the temperatures that the carbide transformation takes place is <30 min.

3.7. Elastic modulus measurements

Elastic modulus measurements showed an irreversible change in modulus at a temperature range between 400 °C and 800 °C, Fig. 11. After the first heating cycle and corresponding measurement there is an irreversible change in the Young's modulus in the temperature range between approximately 400 °C and 800 °C. Subsequent measurements show no change in the Young's modulus results for either the heating or cooling measurement cycles. This change in elastic modulus corresponds with the increase in crack density shown in Fig. 7 and the first exothermic reaction identified in the DSC analysis in Fig. 4, and its

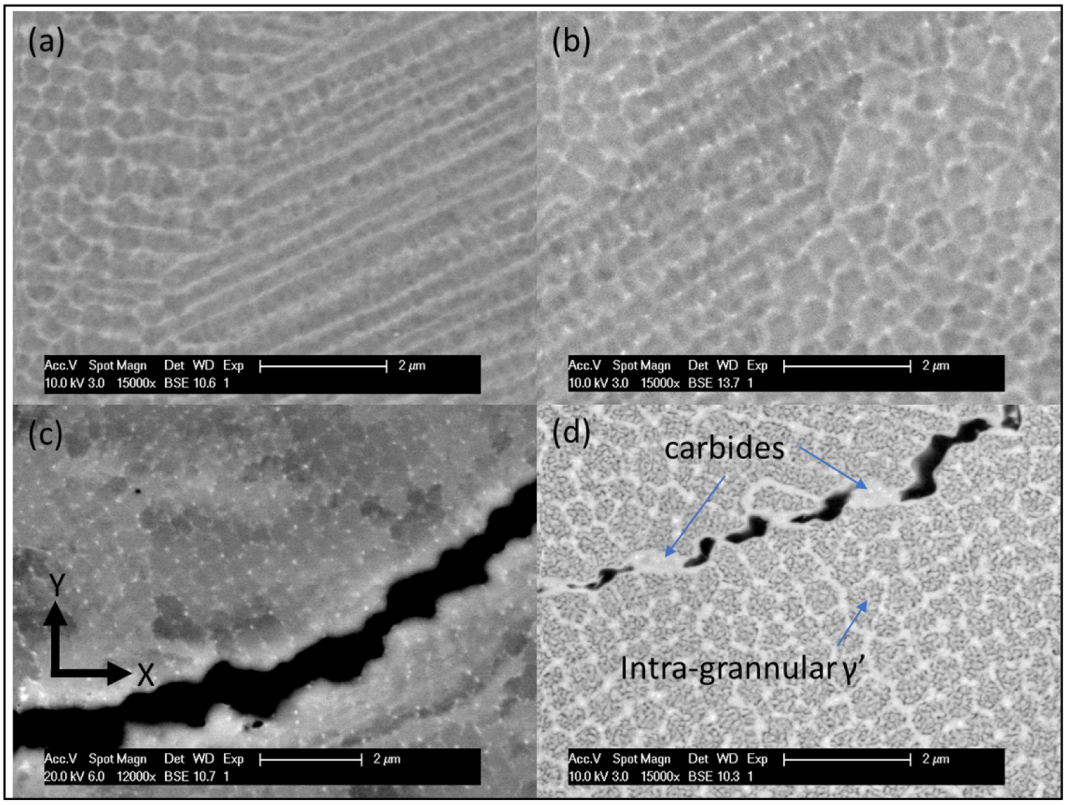

Fig. 9. BSE SEM images transverse to build plane: (a) HT01 2 h at 450 °C, (b) HT02 2 h at 600 °C, (c) HT04 2 h at 750 °C, and (d) HT05 2 h at 850 °C.

associated microstructural changes as identified by the short heat treatments. No phase changes or increases in micro-hardness were observed below 700 °C resulting from the post build heat treatments.

It should be noted that the results from F1-Cool, F1/2 Heat and F1/2 Cool are superimposed, as there is no deviation in the values of Young's modulus following the first heat up cycle represented by F1-Heat. The crystallographic orientation parallel to the build direction has a strong (001) texture [4,9,14], hence the value of Young's modulus is low compared to the isotropic value for this material. Recovery through dislocation movement and grain boundary rotations [31], as well as recrystallisation at higher temperatures, results in a reduction in the crystallographic texture and an increase in Young's modulus parallel to the build direction. Coakley and Dye [32] reported that the modulus of (100) planes in CM247LC is ~179 GPa, compared to a bulk (isotropic) modulus of 259 GPa.

3.8. Thermo-calc results

The results of the equilibrium analysis are shown in Fig. 12 and the predicted phase content in mole fraction is presented in Table 5. The equilibrium γ′ content at 450 °C is 72% decreasing to 52% at 975 °C. The principal carbide phases are MC and $M_{23}C_6$, the $M_{23}C_6$ dissolution temperature is 752 °C. The reduction in $M_{23}C_6$ corresponds to an increase in MC carbide and M_3B_2 borides. The results contrast with the non-equilibrium microstructures seen in as-built LPBF CM247LC, which has a γ microstructure with low volume fractions of nano-sized γ′ precipitates and fine MC carbides at cell and grain boundaries [4,9].

The corresponding Scheil analysis shown in Fig. 13, shows the sequence of phases formed during solidification and their corresponding mole fractions. The first phase to form from the liquid is the γ, identified as FCC_A1, followed by γ + MC, the face centred cubic MC phase is FCC_A1#2, and γ + MC + γ′. The remaining phases predicted are BCC_A2, BCC_B2, P and σ. This data compares with the solidification phase reactions identified in a similar alloy, cast MAR-M002, by Wills and McCartney [30], which showed the sequence of phase growth to be γ, γ + MC followed by the final phase reaction γ + MC + γ/γ′ eutectic.

The microstructures predicted by the Scheil analysis presented in Fig. 13 also compares to the findings of the LPBF microstructures for CM247LC investigated by Wang et al. [4]. The LPBF microstructure consists of γ cells, or dendrites, with fine MC carbides and γ/γ′ eutectic. This suggests the solidification phases formed during LPBF are the same as the cast solidification phases identified by Wills and McCartney [30], although the proportions of the phases will be different due to the high solidification rates in the LPBF process.

3.9. Post build thermal heat treatment cracking

Examination of cracking in sample HT02 (600 °C, 2 h) showed evidence of cracking at grain boundary triple points, fine carbides, and grain boundary sliding, which are all associated with DDC cracking, Fig. 14. Cracking at high angle grains, grain boundary triple points and voids forming close to grain boundary triple points is consistent with the evidence presented in previous work carried out on Ni-superalloy welds [16,33], which showed that DDC could initiate at temperature as low as 700 °C in Ni-superalloy welds.

During grain boundary sliding, cracks are formed at grain boundary irregularities, such as carbides, or triple points [34]. The serrated appearance of the crack faces seen in Fig. 14(c) is clearly indicative of this type of failure. The main difficulty in distinguishing DDC, caused by grain boundary sliding, from other grain boundary fracture mechanisms is that they are both associated with grain boundary carbides phases. Cavitation or fracture occurs at grain boundary carbides due to localised stress concentrations. Cracking is limited to straight sections of grain boundaries, whereas more tortuous grain boundaries appear to be more resistant to DDC cracking. LPBF produces a columnar grain structure along the build direction, which would be more susceptible to DDC cracking than tortuous or equiaxed grain structures.

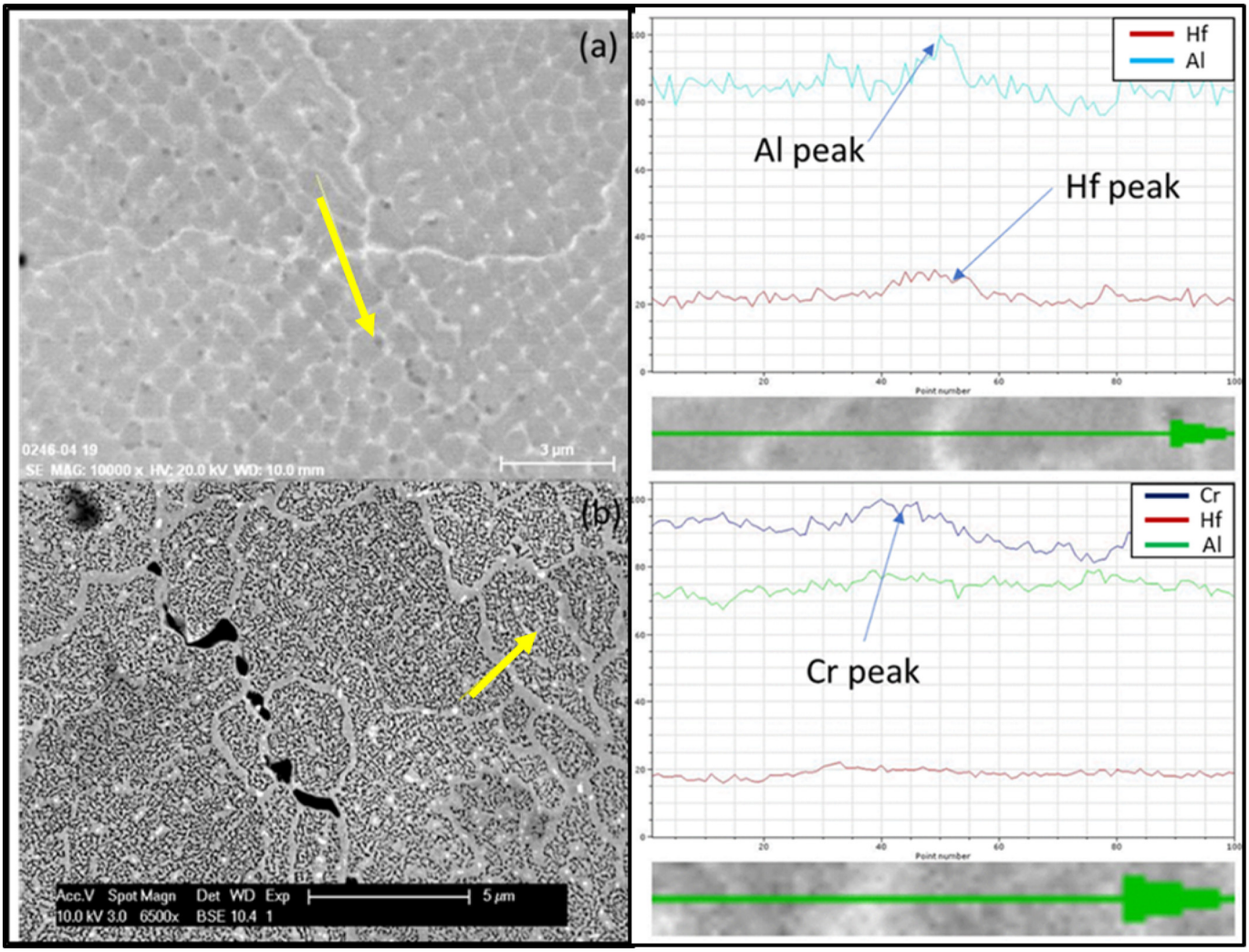

Fig. 10. EDS analysis (a) HT02 600 °C for 2 h, Al and Hf peaks detected at grain boundaries, (b) HT06 no change in Al and Hf concentration due to precipitation of γ′ phase within cells and at grain boundaries. Cr peak indicates growth of $M_{23}C_6$ carbides.

Crystallographic orientation has also been shown to affect DDC; it was stated, based on the work by Bowers, Kikel and Parker [35,36] that grain orientation had a notable effect on the susceptibility to DDC cracking, the strain threshold for DDC reduced from 2.5% strain to 1% strain in the presence of high angle grain boundaries. The first stages of recovery involve rotations of low angle grain boundaries [31,37]. Local variations in crystallographic orientation have been identified by Munoz-Moreno et al. [14]. Therefore, both the increase in DDC cracking and the change in Young's modulus indicate the onset of recovery at lower temperatures. The evidence from the experiments, including the increase in crack density, the change in elastic modulus, and the microstructural evidence of grain boundary sliding are all associated with DDC.

Precipitation of γ′ phase and growth of grain boundary carbides at temperatures above 750 °C retards grain boundary sliding, increased the micro-hardness, and reduces micro-cracking, but leads to SAC. The probable cause of the increase in crack density at 975 °C is due to creep cavitation and cracking resulting from residual stresses generated during build, Fig. 15. Although both DDC and creep fracture are associated with cracking along grain boundaries, the formation and coalescence of voids along grain boundaries, shown in Fig. 15, is a clear indication of intergranular fracture resulting from Power Law creep [38]. The reduction in micro-hardness at 975 °C could result from either reduced γ′ volume fraction, supported by evidence from the Thermo-Calc analysis, or a reduction in residual stress due to creep. Microstructural evidence from HT05 and HT06 does not suggest a decrease in γ′ content at the higher heat treatment temperature.

4. Conclusions

Different modes of crack formation have been identified during post build heat treatments in LPBF CM247LC, which are associated with two distinct exothermic reactions associated with changes in elastic modulus, phase changes including growth of intergranular and fine intragranular γ′ phase.

- There is no increase in micro-hardness HV(1) below 700 °C, therefore, the most likely cause for the change in state is due to crystallographic rotations at cell and grain boundaries. These transformations are associated with the normal recovery process in metals and are facilitated by the high dislocation densities and residual stresses generated during the LPBF process.
- The second exothermic peak is associated with the growth of fine inter-cellular γ′ and grain boundary γ′ films. Evidence is provided by the precipitation of the γ′ phase both at grain boundaries and within the cells.
- The growth of γ′ and carbides at cell boundaries prevent alleviation of residual stresses through grain boundary sliding and micro-cracking leading to SAC at temperatures above 750 °C. This is because the

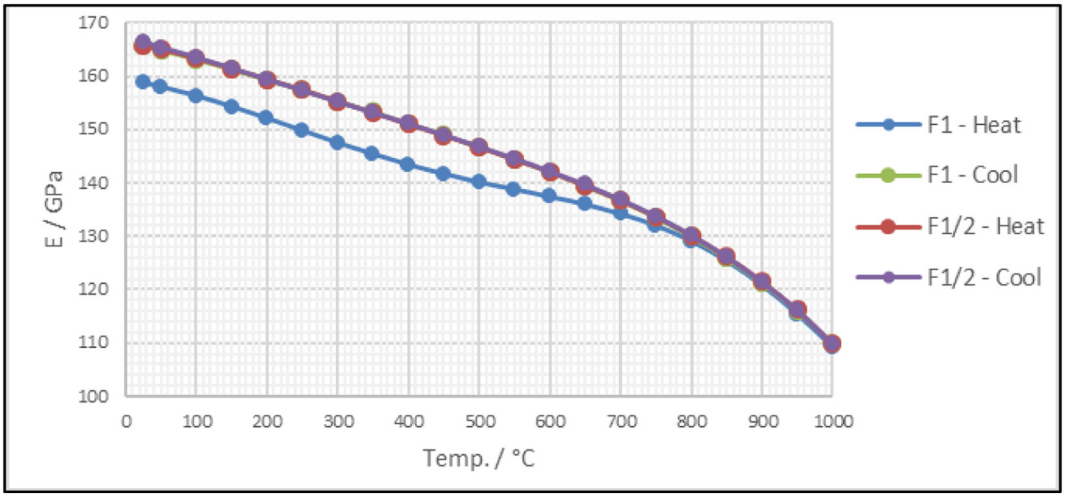

Fig. 11. Young's modulus measured parallel to the LPBF build direction, measurement F1 Heat is the first measurement from RT to 1000 °C, F1 Cool, measurements cooling from 1000 °C to RT, F1/2 Heat, second measurement from RT and F1/cool is the second measurement cooling from 1000 °C.

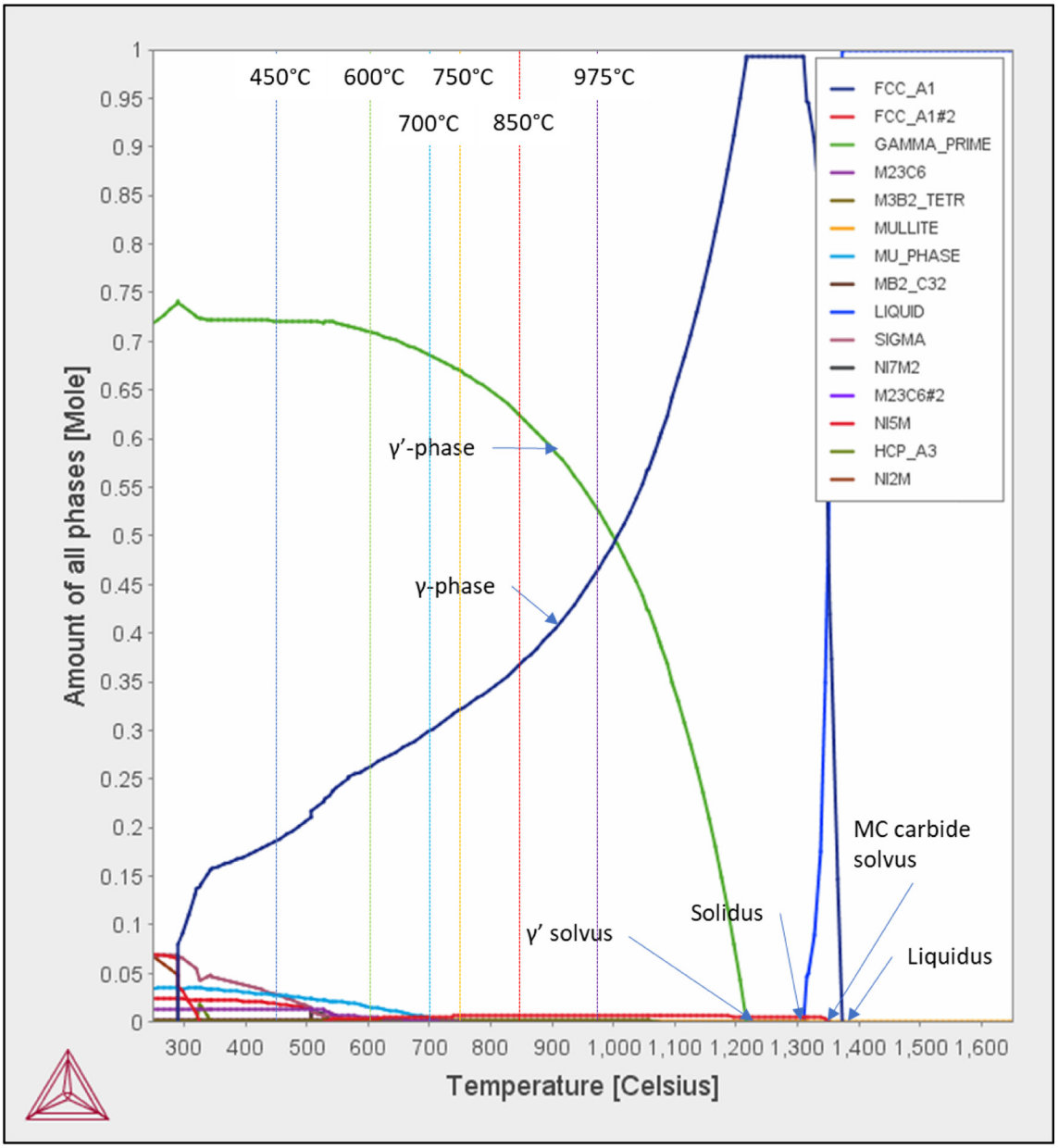

Fig. 12. Mole fraction of phases as a function of temperature for nominal composition CM247LC using TCNI8 database.

Table 5
Mole fractions of phases for CM247LC corresponding to the heat treatment temperatures used in the experiments.

T/°C	FCC γ/mole	σ/mole	γ′/mole	μ/mole	Ni_5M/mole	$M_{23}C_6$/mole	MC/mole	M_3B_2 TETR/mole	$M_{23}C_6$#2/mole
447	0.1852	0.0292	0.7212	0.0279	0.0193	0.0129		0.0017	0.0018
597	0.2607		0.7108	0.0166		0.0054	0.0039	0.0019	
697	0.2978		0.6875	0.0051		0.0017	0.0055	0.0019	
752	0.3225		0.6687			0.0000	0.0062	0.0019	
847	0.3668		0.6245				0.0061	0.0019	
977	0.4670		0.5244				0.0061	0.0019	

precipitation of these phases increases the creep resistance of the material, which means that that low temperature creep mechanisms, such as grain boundary sliding, are suppressed leading to failure by tensile overload. This phenomenon is demonstrated in LPBF component builds, especially in high temperature alloys such as CM247LC. This is the primary reason for post build shot blasting or peening proposed in the LPBF manufacturing patent by Illston [13]. The post build surface treatment imparts compressive residual stress in the surface of the build, which retards cracking, by any of the identified mechanisms, during post build HIP.

- At 975 °C micro-cracking increases, the mechanism for crack formation is creep identified by grain boundary cavitation and crack growth.

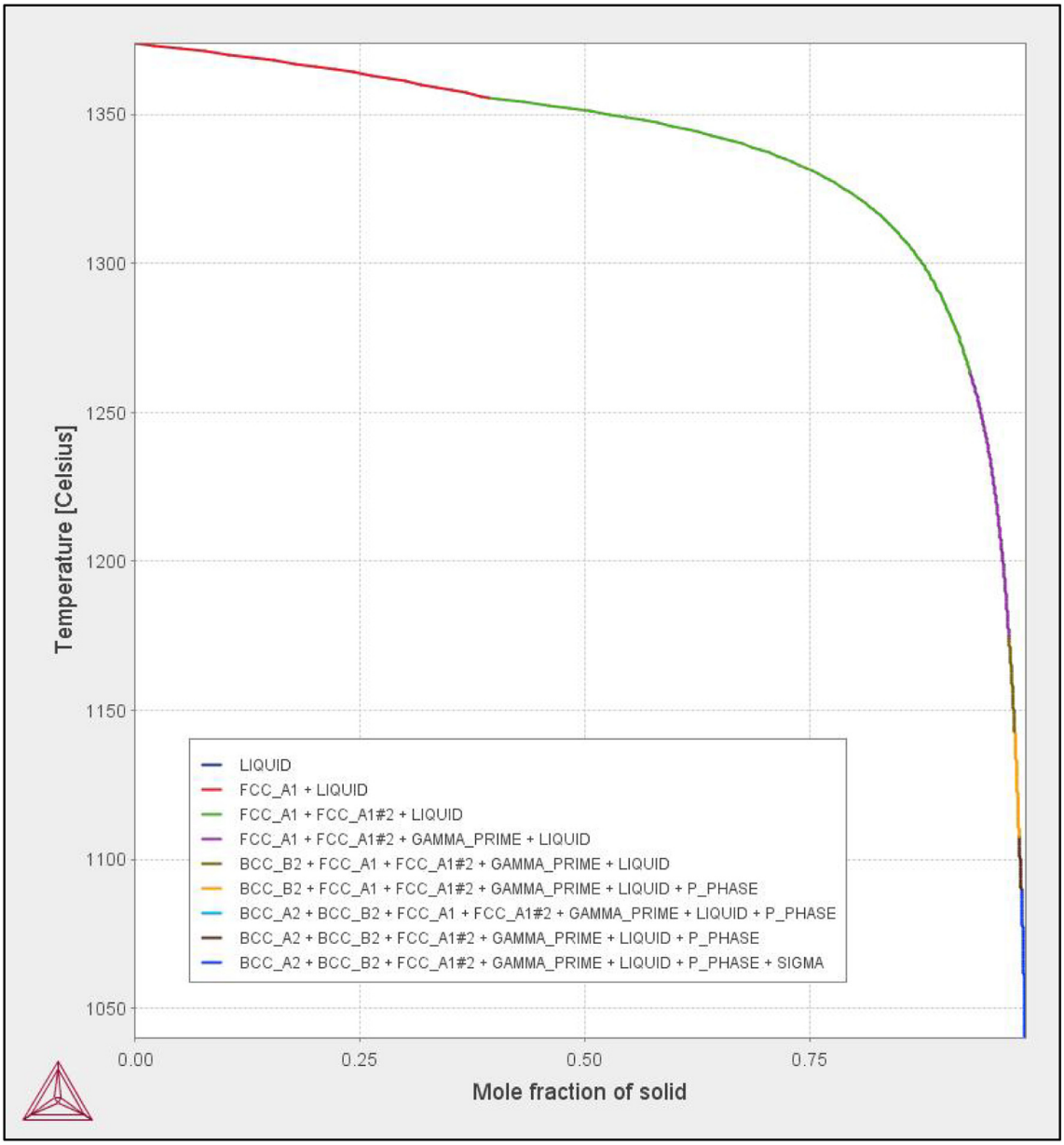

Fig. 13. Reactions during solidification showing mole fractions of phases and their sequence of formation.

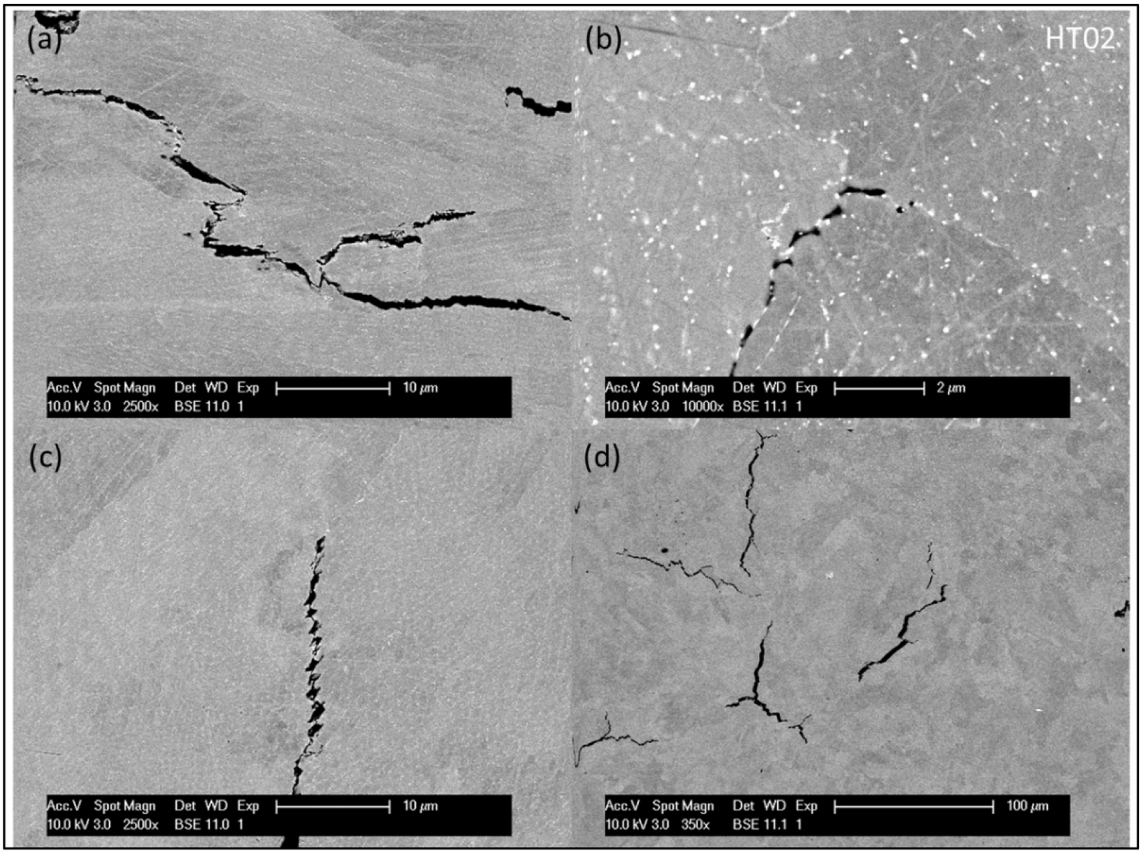

Fig. 14. Post build heat treatment cracking: (a) HT02 600 °C 2 h BSE image showing triple point cracking in a section taken paralleled to the build plane, (b) grain boundary cracking associated with grain boundary carbides perpendicular to the build plane, (c) tearing at grain boundary due to grain boundary sliding, (d) triple point cracking.

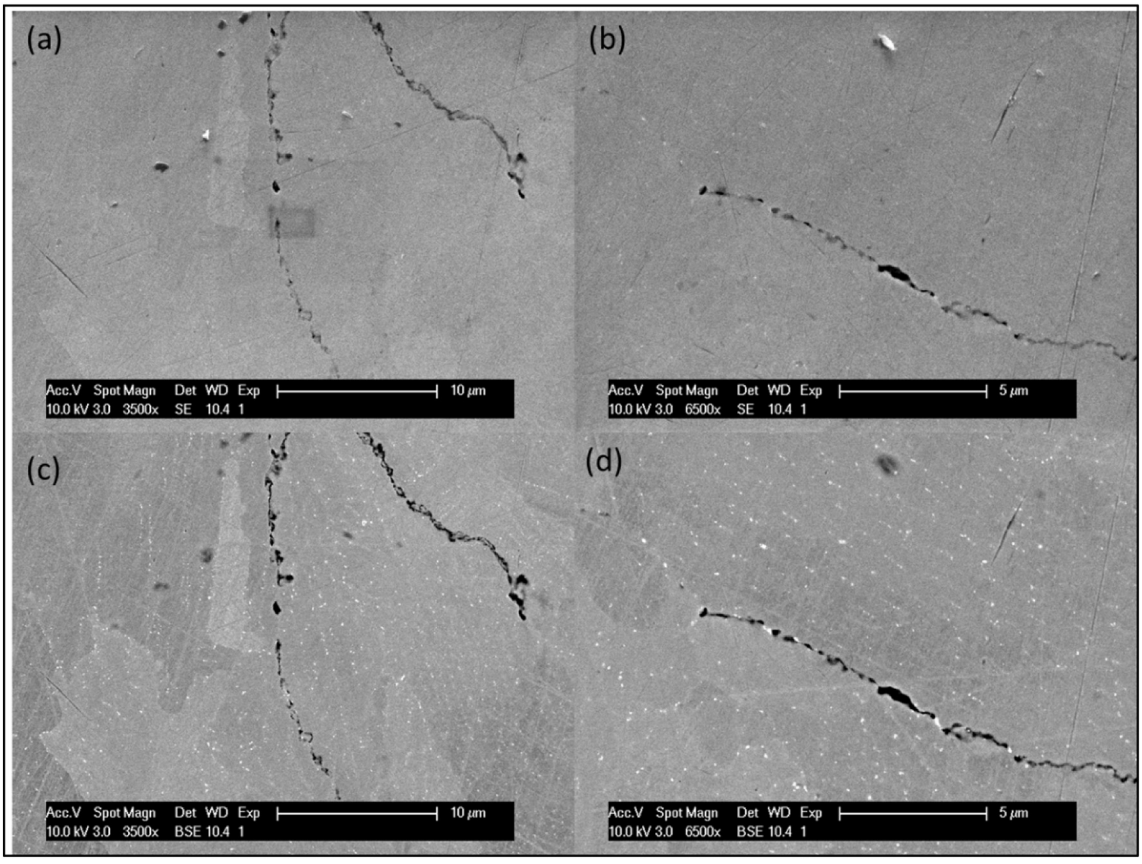

Fig. 15. Creep cavitation at grain boundaries: (a, c) as polished SE and BSE image HT06, 975 °C 2 h, (b, d) close-up of cracks showing grain boundary creep cavitation, SE and BSE image.

The presence of oxygen, even in low concentrations, at elevated temperatures will accelerate the creep crack growth rate during post-LPBF heat treatment processes.
- All the cracking mechanisms are driven by the high residual stresses and the microstructural development, which are a consequence of the rapid cooling rates associated with the LPBF.
- Low temperature annealing may be possible as it will relieve the constraint imposed by the steel baseplate, however it has been shown that the low temperature annealing at temperatures below 700 °C will lead to increased micro-cracking.

5. Further work

Many of the changes in microstructure and crystallographic texture during the heat treatment experiments are not observable using SEM. Therefore, further proof of the conclusions proposed in this study can be reinforced by TEM analysis. The results could be used to design a post-LPBF heat treatment that does not exacerbate cracking, and maximises the build strength.

Credit author statement

JHB performed the experimental work during his MSc research at the University of Birmingham, which was supervised by MMA. DC and WL provided industrial insight into the work, and co-supervised the project.

Acknowledgements

The authors would like to acknowledge the use of elastic modulus and residual stress data provided through EU Project MERLIN funded by the European Commission, contract ACPO-GA-2010-266271. John H. Boswell acknowledges the support from the Royal Academy of Engineering for funding his MSc by research programme at the University of Birmingham.

References

[1] K.E. Harris, GL, R.E. Schwer, Development of high creep strength, high ductility, cast Superalloy for integral turbine wheels CM247LC(R), AIME Annual Meeting 1982, Cannon-Muskegon Corporation, 1982.
[2] G.H.,.K. Erickson, R.E. Schwer, DS CM247 LC Characteristic Properties with Optimized Solutioning Techniques, in Gas Turbine Conference and Exhibit, The American Society of Mechanical Engineers, Houston, Texas, USA, 1985 1–16.
[3] G.K. Cam, M, Progress in joining of advanced materials, Int. Mater. Rev. 43 (1) (1998) 1–44.
[4] X.C.L. Wang, B. Pang, M. Attallah, M. Loretto, Microstructure and yield strength of SLM-fabricated CM247LC Ni-superalloy, Acta Mater. 128 (2017) 87–95.
[5] L.A. Carter, R. M Reed, Laser powder bed fabrication of nickel-base Superalloys: characterization, quantification and mitigation of cracking, Superalloys (2012) 557–586.
[6] R.E.T. Engeli, S. Hovel, K. Wegener, Processibility of different IN738LC powder batches by selective laser melting, J. Mater. Process. Technol. 229 (2016) 484–491.
[7] D.M.W. Gu, K. Wissenbach, R. Proprawe, Laser additive manufacturing of metallic components: materials, processes and mechanisms, Int. Mater. Rev. 57 (2012) 133–164.
[8] K.G. Amato, L. S; Murr, E. Martinez, P. Shindo, J. Hernandez, S. Collins, F. Medina, Microstructures and mechanical behavior of Inconel 718 fabricated by selective laser melting, Acta Mater. 60 (2012) 11.
[9] V.D.M.-M.R. Divya, O.M.D.M. Messé, J.S. Barnard, S. Baker, T. Illston, H.J. Stone, Microstructure of selective laser melted CM247LC nickel-based superalloy and its evolution through heat treatment, Mater. Charact. 114 (2016) 62–74.
[10] M.C. Grasso, BM, Process defects and in situ monitoring methods in metal powder bed fusion: A review, Meas. Sci. Technol. 28 (2017) 4.
[11] F.W.X.H. Wang, D. Clark, On direct laser deposited Hastelloy X: dimension, surface finish, microstructure and mechanical properties, Mater. Sci. Technol. (2010) 1–13.
[12] J. Boswell, Development of Aero Engine Component Manufacturing Using Laser Additive Manufacturing, in MERLIN, European Commission, 2014.
[13] T. Illston, in: U.P. Office (Ed.), Additve Manufacturing, Materials Solutions, United States 2014, pp. 1–10.
[14] Muñoz-Moreno, R.D., VD; Driver, SL; Messe, OMDM; Illston, T; Baker, S; Carpenter, MA; Stone, HJ, Effect of heat treatment on the microstructure, texture and elastic anisotropy of the nickel-based superalloy CM247LC processed by selective laser melting. Mater. Sci. Eng. A, 2016. 674: p. 529–539.
[15] T.E.R. Etter, A. Kuenzler, in: U.P. Office (Ed.), Method for Post Built Heat Treatment of Additively Manufactured Components Made of Gamma-Prime Strenghtened Superalloys, Alstom Technologies Ltd, United States 2015, pp. 1–9.
[16] Collins, M.L., JC, An investigation of ductility dip cracking in nickel-based filler materials — part I. Welding Research, 2003: p. 288–295.
[17] L.N. Carter, et al., Process optimisation of selective laser melting using energy density model for nickel based superalloys, Mater. Sci. Technol. 32 (7) (2016) 657–661.
[18] Materials, A.S.f.T.a, Standard Test Method for Determining Residual Stresses by the Hole-Drilling Strain-Gage Method, ASTM International, West Conshohocken, Pennsylvania, United States, 2013.
[19] J.W. Lodge, PH, Laser Sintered Samples in CM247LC Residual Stress Assessment; Orthotropic Material Properties, Stresscraft Ltd., 2015 1–11.
[20] R. Morrel, High Temperature Elastic Modulus Characterisation of Laser Deposited CM247LC Nickel Alloy, National Physical Laboratory, Teddington, Middlesex, UK, 2014 1–40.
[21] F.a. Kurz, Fundamentals of Solidification, Trans Tech Publications, Zurich, 1998.
[22] Q.T.S. Li, H. Yu, N. Tian, Y. Su, Y. Li, Effects of carbides and its evolution on creep properties of a directionally solidified nickel-based superalloy, Materials Science & Engineering A 633 (2015) 20–27.
[23] Kim, I.S.C., B.G; Hong, H.U; Yoo, Y.S; Jo, C.Y, Anomalous deformation behavior and twin formation of Ni-base superalloys at the intermediate temperatures. Mater. Sci. Eng. A, 2011. 528: p. 7149–7155.
[24] P.K. Mercelis, J-P, Residual stresses in selective laser sintering and selective laser melting, Rapid Prototyp. J. 12 (5) (2006) 254–265.
[25] A.M.B.B. Beyer, T. Vasco, High-speed tool steels, in: A. International (Ed.), ASM Hand Book Machining, ASM International, Russell Township, Ohio, US 1989, pp. 51–59.
[26] . Vilaro, T.C., C.; Bartout, J.D.; Naze, L.; Sennour, M., Microstructural and mechanical approaches of the selective laser melting process applied to a nickel-base superalloy. Mater. Sci. Eng. A, 2012. 534: p. 446–451.
[27] X.G.J.T. Qin, C. Yuan, C.L. Chen, J.S. Hou, H.Q. Ye, Decomposition of primary MC carbide and its effects on the fracture behaviors of a cast Ni-base superalloy, Mater. Sci. Eng. A 486 (2008) 74–79.
[28] F.B.Y. Royer, Study of the departure from equilibrium and of the thermal behavior of Ni-based superalloy powders and dense materials manufactured by selective laser melting, Armines (2014) 1–10.
[29] Y.L.O.O.A. Wang, R.G. Ding, M.C. Chaturvedi, Weld metal cracking in laser beam welded single crystal nickel base superalloys, Mater. Sci. Technol. 25 (2009) 68–75.
[30] V.M.D.G. Wills, A comparative study of solidification features in nickel base superalloys: microstructural evolution and microsegregation, Mater. Sci. Eng. A145 (1991) 223–232.
[31] B. Ralph, Grain growth, Mater. Sci. Technol. 6 (1990) 1139–1145.
[32] J. Coakley, D. Dye, Lattice strain evolution in a high volume fraction polycrystal nickel superalloy, Scr. Mater. 67 (2012) 435–438.
[33] A.J.S.,.J.B. Ramirez, J.C. Lippold, Improving the ductility-dip cracking resistance of Ni-base alloys, Materials Process Technology 179 (2006) 212–218.
[34] T. Watanabe, Grain boundary sliding and stress concentrations during creep, Metall. Trans. A. 14A (1983) 531–545.
[35] R. Bowers, Edison Welding Institute: Columbus, Ohio, 1997.
[36] J.M.P.,.D.M. Kikel, Ductility dip cracking susceptibility of filler metal 52 and alloy 690, Trends in Welding Research 1998, pp. 757–762.
[37] A.P.S. Haslam, D. Wolf, D. Moldovan, H. Gleiter, Mechanisms of grain growth in nanocrystalline fcc metals by molecular-dynamics simulation, Mater. Sci. Eng. 318 (2001) 293–312.
[38] G.A. Edward, MF, Intergranular fracture during power law creep, Acta Metall. 27 (1979) 1505–1518.